DOI: 10.1002/((please add manuscript number))
Article type: Communication

Guided-mode resonances in all-dielectric terahertz metasurfaces

*Song Han, Mikhail V. Rybin, Prakash Pitchappa, Yuri S. Kivshar, and Ranjan Singh**

Song Han, Dr. Prakash Pitchappa, and Prof. Ranjan Singh
Division of Physics and Applied Physics, School of Physical and Mathematical Sciences,
Nanyang Technological University, Singapore 637371, Singapore

Song Han, Dr. Prakash Pitchappa, and Prof. Ranjan Singh
Centre for Disruptive Photonic Technologies, The Photonics Institute,
Nanyang Technological University, Singapore 639798, Singapore
E-mail: *ranjans@ntu.edu.sg*

Dr. Mikhail V. Rybin
Ioffe Institute, St Petersburg 194021, Russia

Dr. Mikhail V. Rybin, Prof. Yuri S. Kivshar
ITMO University, St Petersburg 197101, Russia

Prof. Yuri S. Kivshar
Nonlinear Physics Center, Australian National University, Canberra ACT 2601, Australia

Keywords: ((terahertz, all-dielectric metasurface, guided-mode resonance, bound states in the continuum))

Abstract

Coupling wave diffractions with the waveguided mode gives rise to the guided mode resonances (GMRs). The GMRs provide designer linewidth and resonance intensity amidst a broad background, and thus have been widely used for numerous applications in visible and infrared spectral regions. Here, we demonstrate terahertz GMRs in low-loss, all-dielectric metasurfaces, which are periodic square lattices of silicon cuboids on quartz substrates. The silicon cuboid lattice simultaneously acts as a diffraction grating and an in-plane slab waveguide, thereby resulting in the formation of terahertz GMRs. At oblique incidence, two distinct frequency detuned GMRs are observed. The frequency difference between these two GMRs increases with increasing angle of incidence However, extremely small angle of incidence causes destructive interference between these counterpropagating GMRs that leads to a non-radiative *symmetry-protected bound state in the continuum*. GMRs in all-dielectric silicon metasurfaces could have potential applications in the realization of efficient terahertz devices such as high-Q transmission filters with angular spectral selectivity, ultrafast modulators, and free-space couplers.

The resonance phenomena in photonics allow for strong localization of electromagnetic waves that is essential for numerous applications [1-7], such as narrowband filtering [8], out-of-plane wave coupling [9], chemical and biological sensing [10], lasing [11, 12], harmonic generation [13-17], Raman scattering [18], and photovoltaics [19]. The important parameters that describe a resonance feature are its intensity and spectral linewidth. For most practical applications, resonances with strong intensity and narrow linewidth are desirable. Higher resonance intensity provides better signal to noise ratio, while narrower linewidth signifies larger field confinement. However, most of the resonances are constrained by the trade-off between resonance intensity and linewidth [20]. This limits the possibility of independent tailoring of resonance features at will. On the contrary, guided mode resonance (GMR) can provide arbitrary resonance intensity and linewidth through geometrical design and selection of materials [8]. Due to this versatile nature of GMRs, they have found wide range of applications, including extremely high-Q filters, ultra-broadband reflectors, wavelength selective polarizers, and beam splitters [8, 21-32]. The GMR filter primarily comprises of a diffractive grating and an in-plane waveguide. The grating diffracts the incident light and couples it into the waveguide, which propagates as a guided mode. However, this guided mode is designed to be leaky, which then interferes with the free space propagating electromagnetic wave to give rise to the GMRs. Through the selection of material, grating design, dielectric layer thickness, and angle of incidence, GMRs can provide a wide range of spectral features. Currently, the exploration of GMRs is limited to optical and radio frequency regions of the electromagnetic spectrum. However, terahertz (THz) technologies are attracting a lot of attention to cater to the challenges of meeting ever-increasing demand for high-speed wireless communications [33]. THz GMR devices could play a crucial role in communication applications due to its capability for constructing high-Q filters, polarization selective beam splitters, differentiators, integrators, and wavelength division (de)multiplexers

[8]. Earlier reports on THz GMRs were realized through 1D grating elements on quartz substrate [34] and periodic metallic patterns on cyclo-olefin substrates [35]. Here, we experimentally demonstrate silicon-based all-dielectric metasurfaces that support GMRs at THz frequencies. The 2D metasurface, building block with periodic array of subwavelength silicon microstructures, simultaneously acts as the diffraction grating as well as the slab waveguide and hence enables the observation of GMRs. At oblique incidence, two frequency detuned GMRs are observed, which arises from two counterpropagating modes in the slab waveguide. However, at normal incidence, the coupling of these two GMRs leads to a symmetry-protected bound state in the continuum (BIC) with infinite *Q* factor. A detailed investigation of GMRs based on the geometrical parameters of the silicon microstructure and angle of incidence are presented in this work.

The unit cell of the metasurface is a silicon cuboid resonator with length *L*, width *W*, and height *H*, as shown in **Figures 1(a)** and 1(b). The silicon cuboid resonators are fabricated on a quartz substrate ($n_{sub} = 2.14$) at the nodes of a square lattice with lattice constant Λ = 300 μm. High-resistivity silicon (ρ >10000 Ω·cm, n_{si} = 3.48) was chosen, due to its low loss and low dispersion characteristics at THz frequencies [36]. The 2D array of silicon cuboid resonators acts as a grating and more importantly, the silicon metasurface also acts as a homogeneous core layer that support slab waveguide modes, governed by total internal reflection (TIR) [37] (see Supplementary Information for details). Figure 1(c) shows the dispersion of a thin film slab waveguide, where the light line is defined by the dispersion relation $|k| = n\frac{\omega}{c}$, which relates the wavevector (k), frequency (ω), speed of light in vacuum (c), and refractive index of waveguide material (n). The modes that lie above the light line are radiative in nature, while those lying below are guided within the slab waveguide. In the case of patterned silicon layer, the waveguiding criteria of the effective slab waveguide can be

expressed as $k = \frac{\omega}{c} n_g sin(\theta)$, where n_g is the average refractive index of the effective slab waveguide and θ is the angle of incidence at the interface of slab waveguide and top cladding (refractive index of n_c). Since, the slab waveguide is a periodic structure, it leads to the translation symmetry of the band structure in the reciprocal space. In a first approximation, the band structure is a repeated band of homogeneous layer, as shown in Figure 1(c) being enumerated as -1, 0, +1 and so on. Due to band folding, the guided modes now fall above the light line and hence become guided resonances that couple to the radiating modes of the cladding. The combination of the waveguiding criteria (i.e. TIR) and the grating equation provides the critical condition for the realization of GMR, which is given by: $n_c < sin(\theta) - m\frac{\lambda}{\Lambda} < n_g$ [8, 21-34, 37], where Λ is the lattice period, λ is wavelength and frequency is given by $f = c/\lambda$. By solving the GMR equation, a pair of GMRs can be readily achieved as a function of θ (see Supplementary Information for details). In the vicinity of Γ point ($\theta = 0°$), rigorous calculations account for the interaction of these resonance modes, which show either anti-crossing behavior indicating a strong coupling regime [7, 38], or cross-over behavior implying a weak coupling regime [7, 38], as highlighted by the blue and red dispersion curves in Figure 1(e), respectively. Earlier works in photonic crystal membranes show anti-crossing behavior due to the periodic modulation of the dielectric constant, which introduces a gap opening and flattening of the dispersion at the center of the Brillouin zone [38- 40]. The 180º rotational symmetry (C_2) of these structures ensures the modes at the Γ point to be either odd or even. The mode splitting at the Γ point results in existence of pure odd modes, which are decoupled from the propagating modes in the cladding due to the symmetry, and results in a symmetry-protected BIC [5, 41]. However, these interactions in the weak coupling regime (**Figure 1(e)** red curve) for excitation of BIC is not very well understood. Our metasurface

that supports GMRs also provides a platform for the detailed investigation of BIC excitation in the weak coupling regime.

The numerical simulations were carried out using CST microwave studio solver for the angle-resolved transmission spectra of the metasurfaces. The simulated results for silicon cuboid resonators with length L = 270 μm, width W = 180 μm at varying θ are shown in **Figure 2(a)**, and L = 270 μm, width W = 210 μm are shown in Figure 2(b), respectively. Periodic boundary conditions were applied in both *x*- and *y*-directions and TM (E_x, H_y, H_z) polarized wave was employed to excite the metasurface. Both metasurfaces show counter propagating mode splitting as function of the angle of incidence, as shown in Figures 2(a) and 2(b), which implies the observation of GMRs. To fabricate the samples, 1.5 μm-thick SiO_2 was first deposited onto 200 μm-thick silicon wafers. Later, 2 μm-thick photoresist was spin coated and conventional photolithography created metasurface patterns on the photoresist. After developing the patterns, the SiO_2 coated silicon wafers with photoresist structures were stuck to a 1 mm-thick quartz ($n_{Quartz} = 2.14$) substrate using UV glue (NOA 85-Norland Products, Inc., $n_{glue} = 1.48$). Reactive ion etching (RIE) was used to pattern the 1.5 μm-thick SiO_2 layer which acts as a hard mask for the silicon etching. Finally, the deep RIE was carried out to etch silicon to obtain the desired samples [36]. The scanning electron microscope (SEM) images of the fabricated sample are shown in Figure 1(a) and 1(b). Each resonator has a length of L = 270 μm in the *x*-direction, width of W = 210 μm in the *y*-direction, and height of H = 200 μm in the *z*-direction.

The transmission spectra of the all-dielectric metasurfaces were performed using a fiber-based THz time-domain spectroscopy (THz-TDS) system (see Supplementary Information for details). In order to enable experimental observation of high-Q resonances, the time-domain scan should be large enough to provide spectral resolution on the order of the

resonance linewidths. Long scan measurements with THz pulses can be challenging due to the etalon pulse from the substrate. To delay the etalon pulse, we stuck the fabricated samples to a thick quartz (thickness of 10 mm) substrate with an ideal optical contact. This allowed for the maximum scan length of ~157 ps, which corresponds to a frequency resolution of 6.37 GHz and the maximum measurable *Q*-factor of 62.79 at 0.4 THz. Further, the emitted time-domain THz beam is focused to a spot size of 10 mm in diameter by a lens with aperture diameter of 22 mm and focal length of 50 mm. Focusing of THz beam limits the minimum achievable θ of 6.84º. For THz-TDS, the transmitted time-domain signals through the samples were transformed to frequency domain and normalized by the transmission signal through an identical bare quartz substrate as the reference. Therefore, the transmission is given by $|\tilde{T}(\omega)| = |\tilde{E}_s(\omega)/\tilde{E}_R(\omega)|$, where $\tilde{E}_s(\omega)$ and $\tilde{E}_R(\omega)$ are the transmission spectra of sample and reference after Fourier transform, respectively.

As shown in Figure 2(c) and 2(d), the angle-resolved transmission spectra for W = 180 μm and 210 μm were measured by rotating the samples with central angles (Φ) of 0º, ±5º, ±10º, and ±15º. This corresponds to the angles of incidence (θ) of 6.84º, ±11.84º, ±16.84º, and ±21.84º, respectively. Therefore, the normal incidence is absent, and the measured spectra always show non-degenerate GMRs, with the +1-order GMR at lower frequency and -1-order GMR at higher frequency. Due to the C_2 rotational symmetry of the metasurface, the ±1-order GMRs show almost same resonant frequency for the positive and negative θ. It is clearly observed that the mismatch (resonance amplitude and frequency) of ±1-order GMRs becomes obvious as Φ reaches ±15º. The transmission measurements were restricted to the maximum θ of ±21.84º ($|\theta| \leq 21.84º$) as the THz beam gets misaligned from the sample at larger angles due to the presence of thick (11 mm) quartz substrate.

To compare the numerical simulations and experimental measurements with the GMR theory, we extracted GMR trajectories (transmission minima) for the simulated data as shown in Figures 2(a) and 2(b) and experimental data plotted in Figures 2(c) and 2(d). Spectral minima of the ±1-order GMRs are plotted in Figure 2(e) for W = 180 μm and in Figure 2(f) for W = 210 μm, where the gray region shows the theoretically calculated GMRs from $n_c < sin(\theta) - m\frac{\lambda}{\Lambda} < n_g$ (see Supplementary Information for details). Experiments show good agreement with the theoretical calculations and numerical simulations. Some minor deviations are observed, which could originate due to the lower refractive index of the UV glue (n = 1.48) that was used to bond the silicon resonators on quartz substrate. The limited resolution (~6.37 GHz) of our THz-TDS system also restricts the maximum value of measured resonance amplitude. In addition, the presence of diffraction mode at 0.47 THz also results in the non-normal diffractions and the suppression of the normal transmission, which is the main reason for large discrepancy between theory and simulation for -1-order GMR above this frequency, as shown in Figures 2(e) and 2(f). To elucidate the characteristics of GMRs in our metasurface, the electric field (real part of E_z component) was simulated at the resonance frequencies as shown in the inset of Figure 2(e) and 2(f). For θ = 6.84°, the +1-order GMR propagates in -x direction while the -1-order GMR propagates in the +x direction, respectively.

Moreover, the metasurface with W = 210 μm shows an additional resonance around 0.457 THz, which is independent of θ, as shown in Figure 2(b) and 2(d). This additional resonance corresponds to the flat-band of photonic band structure that stems from the nearest-neighbor coupling of the silicon cuboid resonators [11, 36, 42, 43]. In the metasurface, the silicon cuboid resonators are periodically arranged in x-O-y plane, which implies that the magnetic field along y-axis is periodically modulated. The magnetic field remains parallel to the

horizontal plane (*x*-*O*-*y* plane) such that the magnetic coupling between silicon resonators remains constant without dependence on θ. Hence, the resonance induced due to magnetic coupling remains unchanged as θ increases. This resonance mode is not observed in the metasurface with W = 180 μm, owing to the reduced coupling between the nearest neighbors.

We further analyze the interactions between degenerate modes near the Γ point by finely varying the angle of incidence (-5° ≤ θ ≤ 5º). **Figures 3(a)** and 3(b) show the simulated transmission spectra at small angles of incidence for the metasurface with W = 180 μm and 210 μm, respectively. As θ decreases from 5°, the two GMRs for the metasurfaces come close to each other and finally push the transparency peak to the symmetry-protected BIC mode. For metasurface with W = 180 μm, two GMR dips show a "Dirac"-like crossing behavior, indicating that the degenerate modes are in the weak coupling regime (same to Figure 1(e), the red curve), as shown in Figure 3(a). Compared to metasurface with W = 180 μm, the one with W = 210 μm open a small band gap due to enhanced magnetic coupling (same reason for the additional resonance) along *y*-axis [39]. Therefore, two GMRs form an anti-crossing behavior at normal incidence that verifies the strong (enhanced magnetic) coupling (same as Figure 1(e) blue curve), as shown in Figure 3(b). To further analyze the symmetry-protected BICs, we also calculated the Q-factor and average field enhancement $\langle E\rangle/|E_0|$ for both metasurfaces, where E_0 is the incident field amplitude and $\langle E\rangle = \frac{1}{V}\int|\boldsymbol{E}(\boldsymbol{r})|d\boldsymbol{r}$ is the averaged electric field over the resonator volume, $\boldsymbol{E}(\boldsymbol{r})$ is the field distribution in 3D coordinates $\boldsymbol{r} = (x, y, z)$. Figure 3(c) shows that the confined field intensity at the transmission peaks, which is fitted by $I = I_0|sin\theta|^{-2}$, where $I = \langle E\rangle^2/E_0^2$. Figure 3(d) shows the calculated Q-factors of the transmission peaks, which is fitted by $Q = Q_0|sin\theta|^{-2}$. It is interesting to note that, both the field enhancement and Q-factor has the α^{-2} dependence (α is the asymmetry parameter and $\alpha = |sin\theta|$), which diverges to ∞ at

θ = 0°, thereby revealing the symmetry-protected nature of BIC [44]. Hence, GMR is inherently a symmetry-protected BIC system at normal incidence and the trapped modes become leaky, i.e. finite *Q*-factor, and the enhancement of field localization reduces as the angle of incidences goes off-normal.

Furthermore, geometrical parameters of the silicon cuboid resonators play a crucial role in the design of GMRs. Here, the effect of resonator length *L* on the GMRs was studied by varying *L* from 180 μm to 300 μm, while keeping the width constant at 210 μm. **Figures 4(a)** and 4(b) shows the simulated transmission spectra of the metasurface with varying length for θ = 0° and 6.84°, respectively. At normal incidence, a single GMR was observed at 0.45 THz for *L* = 180 μm. With increasing *L*, a continuous redshift of the single GMR was observed, which is due to the increased mode volume of the resonator cavity. For *L* = 300 μm, the degenerated GMRs shift to lower frequency of 0.375 THz. However, for the case of θ = 6.84°, a clear mode splitting was observed around the degenerate GMR frequency for all lengths. Figure 4(c) shows the experimentally measured transmission spectra for the metasurface with increasing *L*. For *L* less than 240 μm, higher frequency branch (-1 order) of the GMR is suppressed due to the interference of the higher order Rayleigh diffraction mode in the system. It is important to note that these Rayleigh diffractions also shift to low frequency accordingly with increasing angle of incidence (see also Supplementary Information for details). Therefore, an ideal design to achieve clear GMRs at large angle of incidence is to increase the geometric length of the silicon cuboid, as shown in the transmission spectra for *L* larger than 240 μm in Figure 4(b). The measured transmission spectra in Figure 4 (c) show similar trends as the numerically simulated transmission spectra in Figure 4 (b) even though the diffraction boundaries are not well resolved. However, the ±1-order GMRs for *L* > 240 μm appear clearly in the transmission spectra, which match well with the numerical simulations.

In summary, we have experimentally demonstrated terahertz guided mode resonances in all-dielectric metasurface consisting of a 2D array of silicon cuboid resonators. The metasurface shows two counterpropagating GMRs at oblique incidence, and the spectral difference between their resonance frequencies increases with increasing angle of incidence. However, at very small angles of incidence ($0° < |\theta| \leq 1°$), the destructive interference between the counter propagating GMRs (± 1-order modes) enable extremely high-Q resonances that eventually leads to *symmetry-protected BICs* with infinite Q factor at normal incidence. Our results present an experimental observation of THz GMRs in 2D all-dielectric metasurfaces. This opens up a new route for realizing efficient on-chip THz communication components, such as wavelength selective polarizer, beam splitters, differentiators, integrators, and wavelength division multiplexers. The use of silicon for dielectric resonators could be readily adopted for the realization of ultrafast control of THz GMRs under optical stimulus. Additionally, the special case of extremely high-Q BICs could have immense practical applications in THz filters, sensors, and harmonic generators.

Supporting Information
Supporting Information is available from the Wiley Online Library or from the author.

Acknowledgements
The authors (S.H., P.P., Y.K.S., and R.S.) acknowledge Singapore Ministry of Education (MOE), Grants MOE2016-T3-1-006, MOE2017-T2-1-110 and RG191/17. M.V.R. and Y.S.K. acknowledge support by the Ministry of Education and Science of the Russian Federation (3.1500.2017/4.6) and the Australian Research Council. Dr. Yogesh Kumar Srivastava is further acknowledged for fabricating the samples.

Received: ((will be filled in by the editorial staff))
Revised: ((will be filled in by the editorial staff))
Published online: ((will be filled in by the editorial staff))

References

[1] B. Luk'yanchuk, N. I. Zheludev, S. A. Maier, N. J. Halas, P. Nordlander, H. Giessen, & C. T. Chong, Nat. Mater. **2010**, *9*, 707.

[2] C. J. Chang-Hasnain, W. Yang, Adv. Opt. Photonics **2012**, *4*, 379.

[3] W. Zhou, D. Zhao, Y. C. Shuai, H. Yang, S. Chuwongin, A. Chadha, J. H. Seo, K. X. Wang, V. Liu, Z. Ma, and S. Fan, Progress in Quantum Electronics, **2014**, *38*, 1.

[4] S. Jahani, Z. Jacob, Nature Nanotech. **2016**, *11*, 23.

[5] C. W. Hsu, B. Zhen, A. D. Stone, J. D. Joannopoulos, M. Soljačić, Nat. Rev. Mater. **2016**, *1*, 16048.

[6] A. I. Kuznetsov, A. E. Miroshnichenko, M. L. Brongersma, Y. S. Kivshar, B. Luk'yanchuk, Science 2016, 354, aag2472.

[7] M. F. Limonov, M. V. Rybin, A. N. Poddubny, Y. S. Kivshar, Nat. Photon. 2017, 11, 543.

[8] G. Quaranta, G. Basset, O. J. Martin, B. Gallinet, Laser Photonics Rev. **2018**, *12*, 1800017.

[9] K. Kintaka, J. Nishii, Y. Imaoka, J. Ohmori, S. Ura, R. Satoh, H. Nishihara, *IEEE Photonics Technol. Lett.* **2004**, *16*, 512.

[10] J. Homola, *Chem. Rev.* 2008, **108**, 462.

[11] A. Kodigala, T. Lepetit, Q. Gu, B. Bahari, Y. Fainman, B. Kanté, Nature **2017**, *541*, 196.

[12] J. S. T. Gongora, A. E. Miroshnichenko, Y. S. Kivshar, A. Fratalocchi, Nat. Commun. **2017**, 8, 15535.

[13] Y. Yang, W. Wang, A. Boulesbaa, I. I. Kravchenko, D. P. Briggs, A. Puretzky, D. Geohegan, J. Valentine, Nano Lett. **2015**, *15*, 7388.

[14] S. Liu, M. B. Sinclair, S. Saravi, G. A. Keeler, Y. Yang, J. Reno, G. M. Peake, F. Setzpfandt, I. Staude, T. Pertsch, I. Brener, Nano Lett. **2016**, *16*, 5426.

[15] G. Grinblat, Y. Li, M. P. Nielsen, R. F. Oulton, S. A. Maier, Nano Lett. **2016**,*16*, 4635.

[16] A. S. Shorokhov, E. V. Melik-Gaykazyan, D. A. Smirnova, B. Hopkins, K. E. Chong, D. Y. Choi, M. R. Shcherbakov, A. E. Miroshnichenko, D. N. Neshev, A. A. Fedyanin, Y. S. Kivshar, Nano Lett. **2016**, *16*, 4857.

[17] T. Shibanuma, G. Grinblat, P. Albella, S. A. Maier, Nano Lett. **2017**, *17*, 2647.

[18] B. B. Li, W. R. Clements, X. C. Yu, K. Shi, Q. Gong, Y. F. Xiao, PNAS **2014**, *111*, 14657.

[19] M. L. Brongersma, Y. Cui, S. Fan, Nat. Mater. **2014**, *13*, 451.

[20] L. Cong, M. Manjappa, N. Xu, I. Al‐Naib, W. Zhang, R. Singh, Adv. Opt. Mater. **2015**, 3, 1537.

[21] M. Shyiq Amin, J. Woong Yoon, R. Magnusson, Appl. Phys. Lett. 2013, 103, 131106.

[22] A.-L. Fehrembach, K. Sharshavina, F. Lemarchand, E. Popov, A. Monmayrant, P. Arguel, O. Gauthier-Lafaye, JOSA A **2017**, 34, 234.

[23] M. Niraula, J. W. Yoon, R. Magnusson, Opt. Express 2014, 22, 25817.

[24] M. Niraula, J. W. Yoon, R. Magnusson, Opt. Express **2015**, 23, 23428.

[25] T. Khaleque, M. J. Uddin, R. Magnusson, Opt. Express **2014**, 22, 12349.

[26] C. F. R. Mateus, M. C. Y. Huang, Y. Deng, A. R. Neureuther, C. J. Chang-Hasnain, IEEE Photonics Technol. Lett. **2004**, 16, 518.

[27] A. Ricciardi, S. Campopiano, A. Cusano, T. F. Krauss, L. O'Faolain, IEEE Photonics J. **2010**, 2, 696.

[28] T. Khaleque, M. J. Uddin, R. Magnusson, Opt. Express 2014, 22, 12349.

[29] R. Magnusson, Opt. Lett. 2014, 39, 4337.

[30] W. Yu, D. Wu, X. Duan, Y. Yi, MRS Adv. 2016, 1, 1683.

[31] R. Magnusson, Opt. Lett. 2013, 38, 989.

[32] Y. H. Ko, R. Magnusson, Optica **2018**, 5, 289.

[33] T. Nagatsuma, G. Ducournau, C. C. Renaud, Nat. Photon. **2016**, 10, 371.

[34] H. S. Bark, G. J. Kim, T. I. Jeon, Sci. Rep. **2018**, 8, 13570.

[35] A. Ferraro, D. C. Zografopoulos, R. Caputo, R. Beccherelli. Sci. Rep. **2018**, 8, 17272.

[36] S. Han, L. Cong, Y. K. Srivastava, B. Qiang, M. V. Rybin, W. X. Lim, Q. J. Wang, Y. S. Kivshar, R. Singh, arXiv preprint 2018 arXiv:1803.01992.

[37] S. S. Wang, R. Magnusson, Appl. Opt. **1993**, *32*, 2606.

[38] B. Peng, S. K. Özdemir, W. Chen, F. Nori, L. Yang, Nat. Commun. **2014**, 5, 5082.

[39] K. Sakoda, Optical properties of photonic crystals. Springer Science & Business Media, **2004**.

[40] F. Lemarchand, A. Sentenac, E. Cambril, H. Giovannini, J. Opt. A: Pure Appl. Opt. **1999**, 1, 545.

[41] C. W. Hsu, B. Zhen, J. Lee, S.-L. Chua, S. G. Johnson, J. D. Joannopoulos, M. Soljacic, Nature **2013**, 499, 188.

[42] T. Lepetit, E. Akmansoy, J.-P. Ganne, J.-M. Lourtioz, Phys. Rev. B **2010**, 82, 195307.

[43] M. V. Rybin, D. S. Filonov, K. B. Samusev, P. A. Belov, Y. S. Kivshar, M. F. Limonov, Nat. Commun. 2015, 6, 10102.

[44] K. Koshelev, S. Lepeshov, M. Liu, A. Bogdanov, Y. Kivshar, Phys. Rev. Lett. **2018**, 121, 193903.

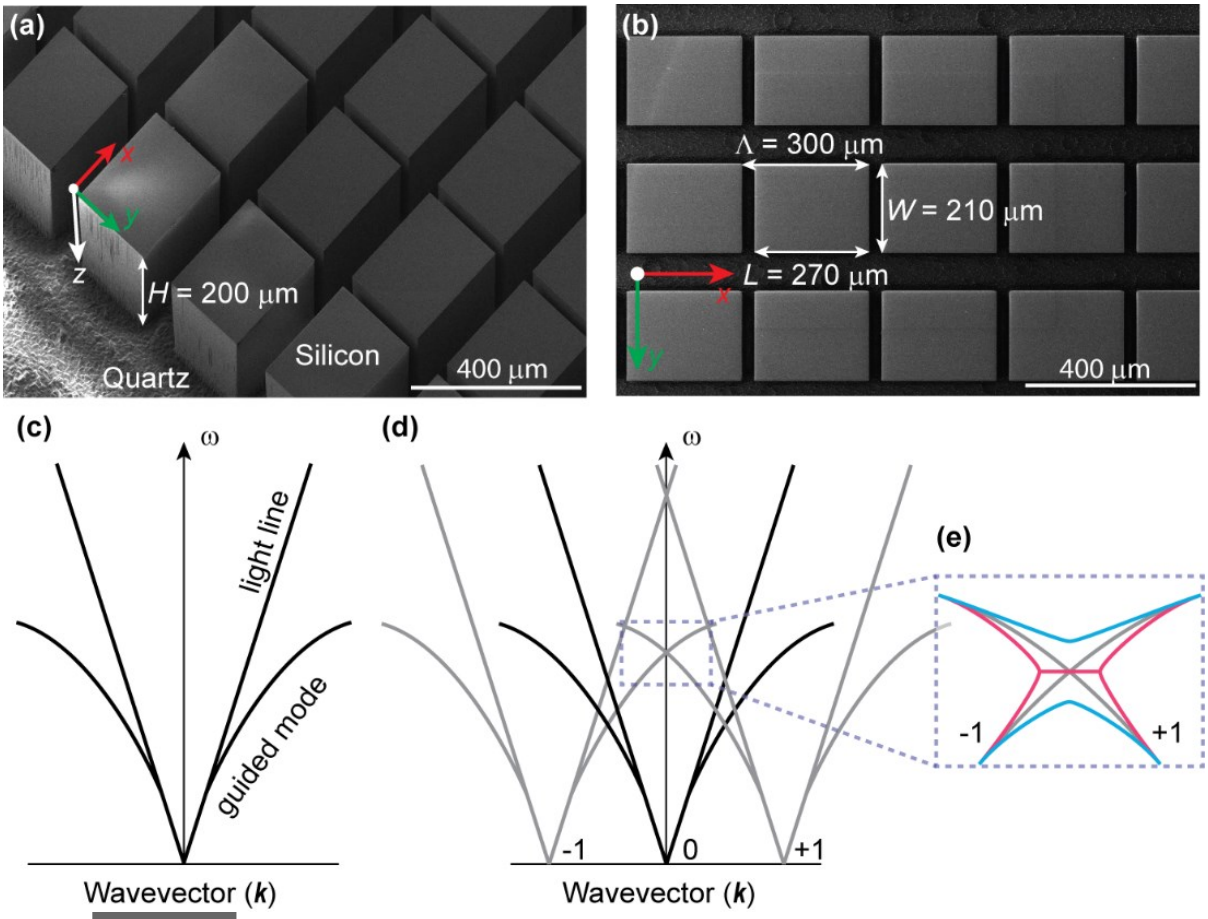

Figure 1. Design of terahertz all-dielectric metasurface for excitation of guided mode resonances (GMRs). (a) Perspective view and (b) Top view of the SEM images of the fabricated metasurface, respectively. The geometrical parameters are lattice constant Λ = 300 μm, length L = 270 μm (along x axis), width W = 210 μm (along y axis), and height H = 200 μm (along z axis). (c) Photonic dispersion curves of the guided modes of the thin film waveguide. (d) Formation of leaky mode above light cone from the band folding of two guided modes from nearest neighbor Brillouin zones. (e) Inset showing the anti-crossing (blue) and cross-over (red) behavior of two eigenmodes, approaching each other that signifies strong coupling and weak coupling regimes, respectively.

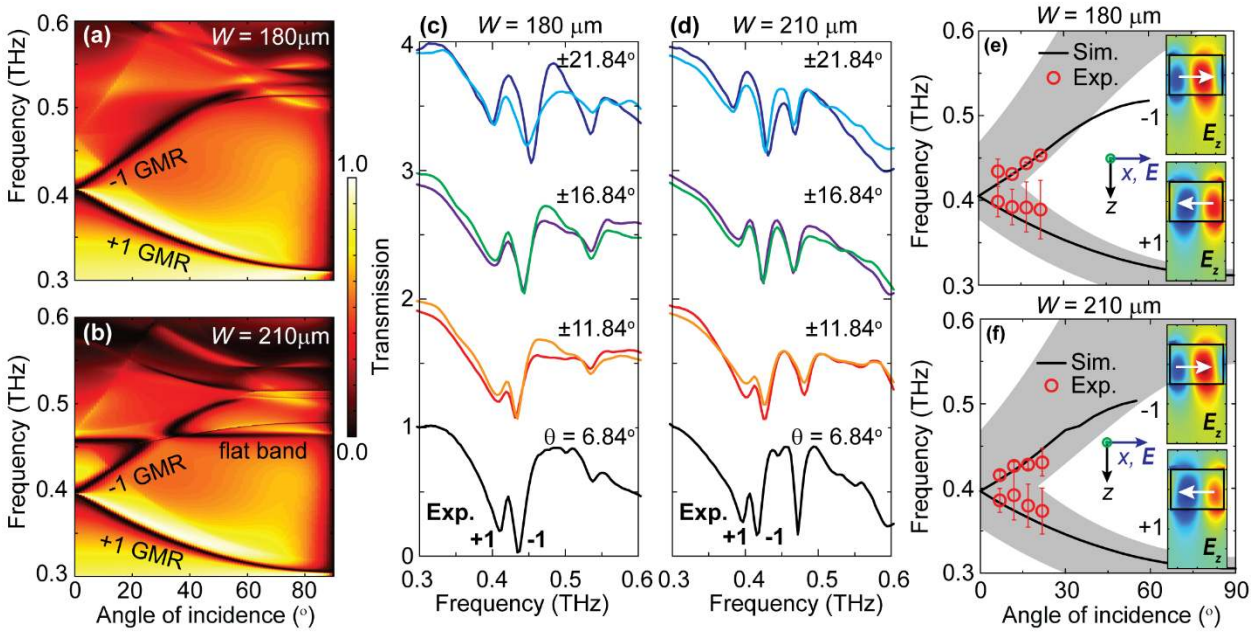

Figure 2. Numerical simulations and experimental measurements of the GMRs in all-dielectric terahertz metasurface. (a), (b) Simulated angle-resolved transmission spectra. The top panel (a) corresponds to the silicon cuboid resonator with geometric parameters of L = 270 μm, W = 180 μm, and the bottom panel (b) corresponds to the silicon cuboid resonator with geometric parameters of L = 270 μm, W = 210 μm, respectively. (c), (d) Experimentally measured transmission spectra at different incidence angles from 6.84° (bottom) to 21.84° (top) for the metasurfaces with W = 180 μm (c) and 210 μm (d), respectively. (e), (f) Corresponding measured transmission spectra as function of angle of incidence for the metasurfaces with W = 180 μm and 210 μm, respectively. The inset figures are the numerically simulated real part of electric field $\boldsymbol{E}_z$ component for +1 and -1 order GMRs at 6.84°, respectively.

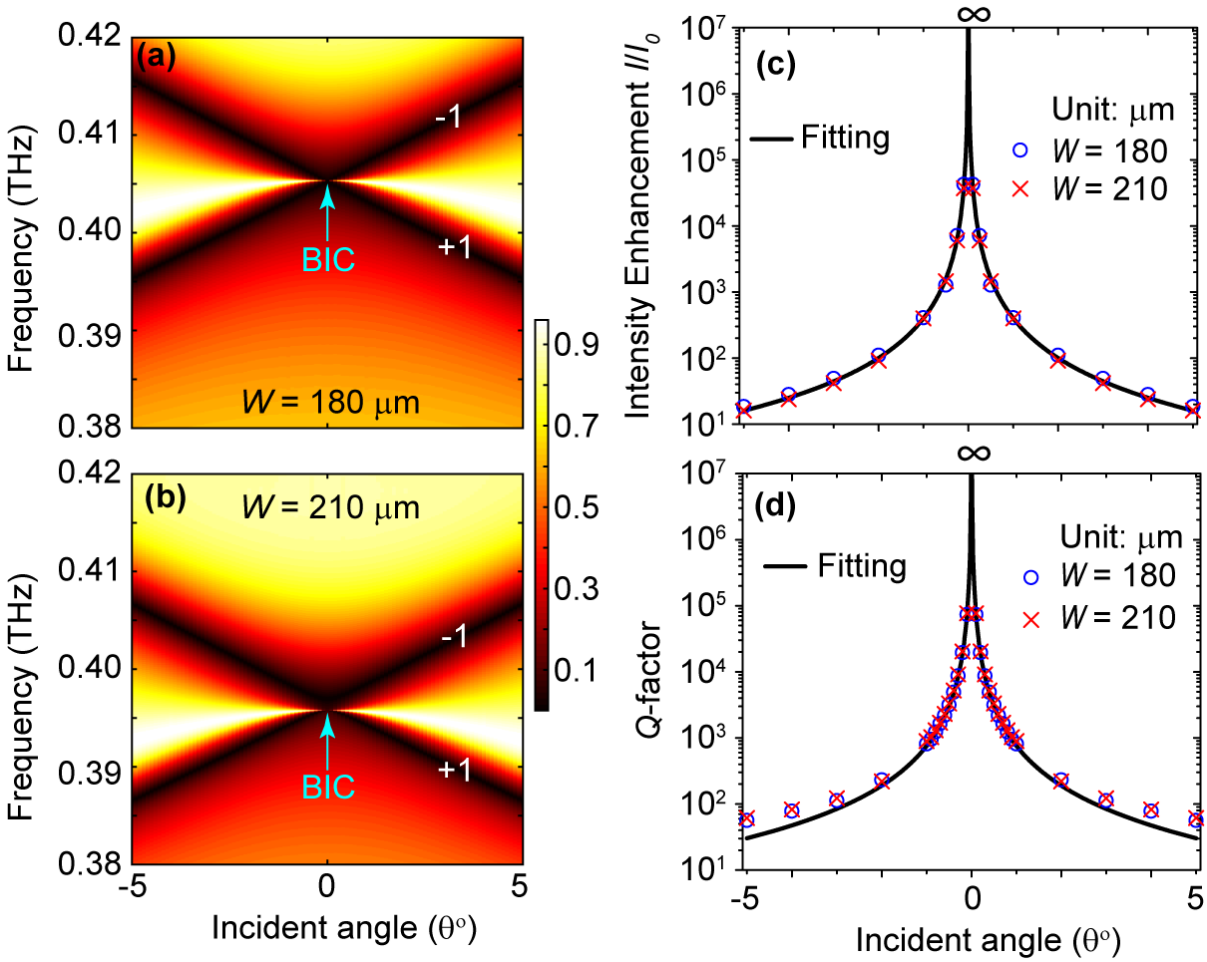

Figure 3. Numerical simulations of the terahertz GMRs near the Γ-point. (a), (b) Calculated transmission spectra for the silicon cuboid with W = 180 μm and W = 210 μm, respectively for angle of incidence from -5° to 5°. (c) Corresponding enhancement of averaged intensity ($\langle E \rangle^2$) inside the silicon cuboid at the transmission peak for small angles of incidence. (d) The calculated Q-factors of the transmission peaks in (a) and (b).

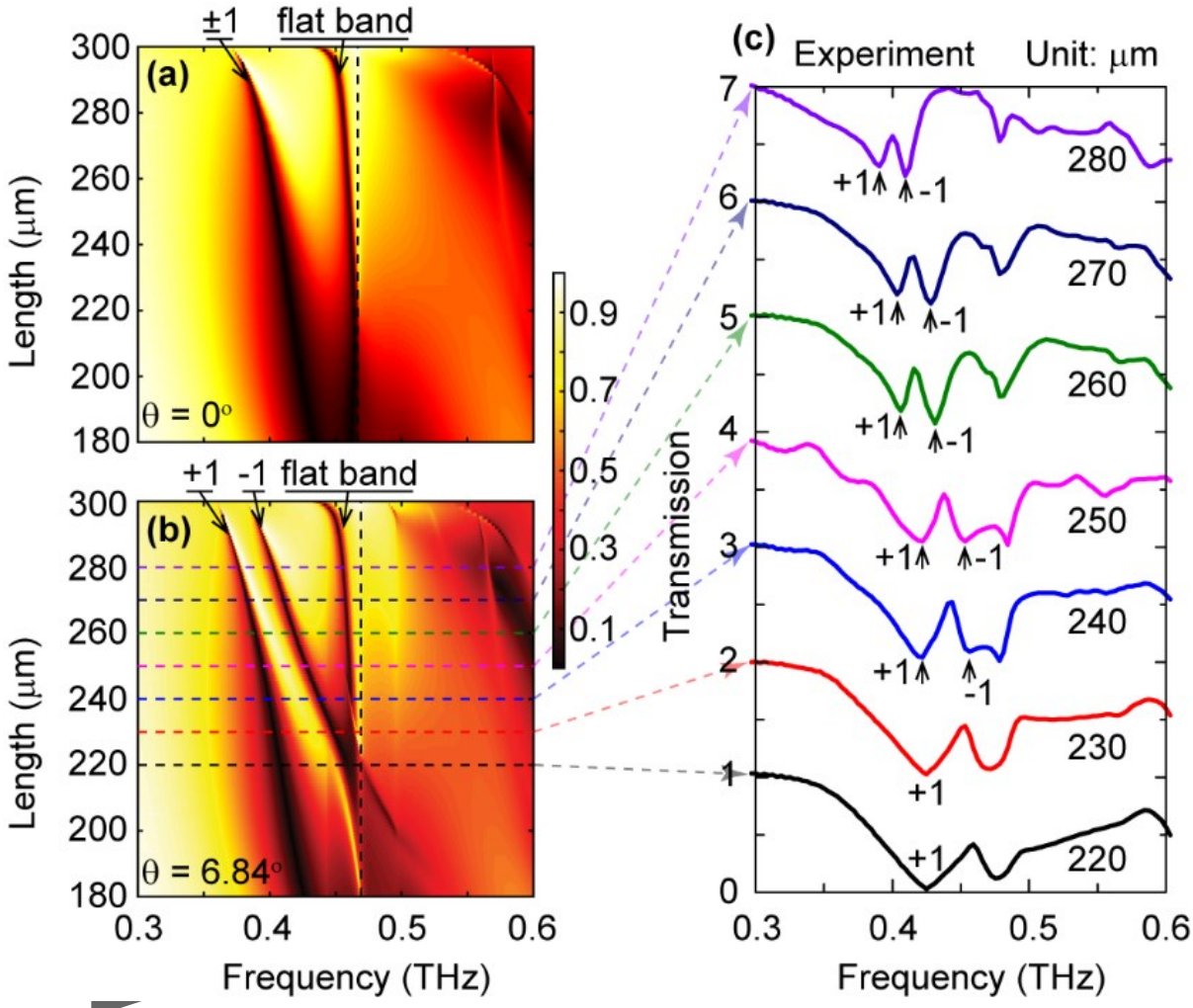

Figure 4. Simulated and measured transmission spectra for terahertz GMRs in metasurfaces with increasing resonator length (L). (a), (b) Simulated transmission spectra of the metasurface with varying silicon cuboid resonator length L for the angle of incidence of 0° (top panel) and 6.84° (bottom panel), respectively. The dashed black line indicates the first-order Rayleigh diffraction mode at 0.468 THz. (c) Measured transmission spectra of the metasurface device at angle of incidence θ = 6.84° by changing length of the silicon cuboid resonator L from 220 μm to 280 μm with a step size of 10 μm.

The table of contents entry should be 50−60 words long, and the first phrase should be bold. The entry should be written in the present tense and impersonal style.

Keyword ((terahertz, all-dielectric metasurface, guided-mode resonance, bound states in the continuum))

*Song Han, Mikhail V. Rybin, Prakash Pitchappa, Yuri S. Kivshar, and Ranjan Singh**

Song Han, Dr. Prakash Pitchappa, and Prof. Ranjan Singh
Division of Physics and Applied Physics, School of Physical and Mathematical Sciences, Nanyang Technological University, Singapore 637371, Singapore

Song Han, Dr. Prakash Pitchappa, and Prof. Ranjan Singh
Centre for Disruptive Photonic Technologies, The Photonics Institute, Nanyang Technological University, Singapore 639798, Singapore
E-mail: *ranjans@ntu.edu.sg*

Dr. Mikhail V. Rybin
Ioffe Institute, St Petersburg 194021, Russia

Dr. Mikhail V. Rybin, Prof. Yuri S. Kivshar
ITMO University, St Petersburg 197101, Russia

Prof. Yuri S. Kivshar
Nonlinear Physics Center, Australian National University, Canberra ACT 2601, Australia

Guided-mode resonances in all-dielectric terahertz metasurfaces
TOC figure ((Please choose one size: 55 mm broad × 50 mm high **or** 110 mm broad × 20 mm high. Please do not use any other dimensions))

TOC Keywords:

Terahertz guided-mode resonance

Table of Contents (TOC) text

Low-loss silicon cuboid based all-dielectric terahertz metasurfaces act simultaneously as diffraction grating and in-plane slab waveguide, thereby enabling excitation of guided mode resonances (GMRs). At normal incidence, destructive interference between counter propagating GMRs give rise to symmetry-protected bound state in the continuum (BIC). Terahertz GMRs are multifunctional devices that could enable narrow-band filters, ultrafast modulators, and free-space couplers.